Progress In Electromagnetics Research, PIER 66, 65–88, 2006

ON THE IMAGE APPROXIMATION FOR ELECTROMAGNETIC WAVE PROPAGATION AND PEC SCATTERING IN CYLINDRICAL HARMONICS

S.-L. Liao and R. J. Vernon

Electrical and Computer Engineering
University of Wisconsin
Madison 53706, USA

Abstract—A closed-form formula, the discrepancy parameter, which has been defined as the ratio of the modal expansion coefficients between the electromagnetic field obtained from the image approximation and the incident electromagnetic field, has been proposed for the evaluation of the validity of the image approximation in the electromagnetic wave propagation, i.e., Love's equivalence principle, and the electromagnetic wave scattering, i.e., the induction equivalent and the physical equivalent, in the cylindrical geometry. The discrepancy parameter is derived through two equivalent methods, i.e., the vector potential method through the cylindrical addition theorem and the dyadic Green's function method, for both the TE and TM cylindrical harmonics. The discrepancy parameter justifies the fact that the image approximation approaches the exact solution for the cylindrical surface of infinite radius. For the narrow-band field with limited spectral component in $\mathbf{k}$ space, the cylindrical modal expansion of the electromagnetic wave into the TE and TM cylindrical harmonics can be separated into the forward-propagating wave that propagates forward and the back-scattered wave that is back-scattered by the PEC surface, within the image approximation. The discrepancy parameter shows that the validity of the image approximation depends on the property of the incident field and the radius of the cylindrical surface, i.e., the narrow-band field and the surface of a large radius are in favor of the image approximation, which has also been confirmed by the numerical result.

1. INTRODUCTION

The image approximation has been frequently used as the approximate solution of Love's equivalence principle for the electromagnetic wave propagation [1–3] and in the induction equivalent and the physical equivalent in the electromagnetic wave scattering phenomenon, which includes microwave imaging [4, 5], reflector antenna design [6, 7], evaluation of Radar Cross Section (RCS) [8, 9] and other applications [10–12]. Recently, the image approximation also finds the application in the mirror system design for quasi-optical mode converters in high-power gyrotrons [13–16]. It is well-known that the image approximation only works well for the smooth surface with a large radius (small curvature), where the equivalent surface currents ($\mathbf{M}_s$, $\mathbf{J}_s$) can be approximated by twice the magnetic surface current ($\mathbf{M}_s^{\text{app}} = 2\mathbf{M}_s$) or twice the electrical surface current ($\mathbf{J}_s^{\text{app}} = 2\mathbf{J}_s$) [1, 3, 17, 18]. However, although the exact solution of the plane wave scattering problem in the cylindrical geometry has been found [17, 19, 20], no general closed-form formula has been reported so far about how large the radius of a cylindrical surface should be in order to achieve an accurate enough image approximation, for the arbitrary incident electromagnetic field. It is helpful to derive such formula in its closed-form expression in order to use the image approximation efficiently.

In this article, the discrepancy parameter due to the image approximation of the electromagnetic wave propagation and scattering has been investigated for the open cylindrical surface and for arbitrary narrow-band field. Non-cylindrical surface can be approximately regarded as the local cylindrical surface with radius defined by the local curvature. The derivation of the discrepancy parameter of the image approximation in the cylindrical geometry can be done through the following steps: 1) specify some arbitrary incident electromagnetic wave in the form of TE and TM cylindrical harmonics on the initial cylindrical surface [20, 21]; 2) apply the image approximation $\mathbf{M}_s^{\text{app}}$ ($\mathbf{J}_s^{\text{app}}$) on Love's equivalence principle in the electromagnetic wave propagation scenario and on the induction equivalent (the physical equivalent) in the electromagnetic wave scattering scenario; 3) calculate the forward-propagating wave (back-scattered wave) on the initial cylindrical surface through either the vector potential method or the dyadic Green's function method; and 4) obtain the ratio of the modal expansion coefficients between the calculated forward-propagating wave (back-scattered wave) calculated from step 3) and those of the initial incident electromagnetic wave given in step 1), which leads to the discrepancy parameter due to the image approximation in the cylindrical geometry.

The rest of this article is organized as follows: Section 2 presents the derivation of the discrepancy parameter due to the image approximation through two equivalent methods, i.e., the vector potential method and the dyadic Green's function method, for both the TE and TM cylindrical harmonics. The numerical result is shown and discussed in Section 3, followed by Section 4, the concluding remarks. The time dependence $e^{i\omega t}$ $(i \equiv \sqrt{-1})$ is used in this article.

2. TWO EQUIVALENT METHODS

The scheme used to illustrate the image approximation for the cylindrical geometry is shown in Fig. 1, where the incident field $\mathbf{E}^i$ propagates onto cylindrical surface S, after which $\mathbf{E}^i$ may continue to propagate to $\mathbf{E}^{>+}$ or it could be back-scattered to $\mathbf{E}_<{}^+$ or $\mathbf{E}^>{}_- = \mathbf{E}_{<-}$, depending on whether it is a forward propagation problem where the Love's equivalence principle can be applied on surface S or a scattering problem where surface S serves as a PEC scatter. Two equivalent methods will be used to obtain the discrepancy parameter due to the image approximation.

The incident field $\mathbf{E}^i$ propagates onto cylindrical surface S with a radius of ρ_0, then it may forward-propagate to $\mathbf{E}^{>+}$ if it is a forward propagation problem; or it could be back-scattered to $\mathbf{E}^>{}_- = \mathbf{E}_{<-}$ if surface S serves as a PEC scatter. $\hat{\mathbf{n}}^+$ and $\hat{\mathbf{n}}^-$ are the outward and inward unit surface normals to S respectively. $\mathbf{M}_s^{\text{app}+}$ and $\mathbf{J}_s^{\text{app}+}$ are the image approximations of the equivalent surface currents for Love's equivalence principle; $\mathbf{M}_s^{\text{app}-}$ and $\mathbf{J}_s^{\text{app}-}$ are the image approximations of the induction equivalent and the physical equivalent respectively. $S^>$ and $S_<$ are surfaces that are infinitesimally close to surface S, from outside $(\rho > \rho_0)$ and from inside $(\rho < \rho_0)$ respectively. The superscript "$^+$" and the subscript "$_-$" denote the front-wave $(y > 0)$ and the back-wave $(y < 0)$; the superscript "$^>$" and the subscript "$_<$" denote the $\rho > \rho_0$ and $\rho < \rho_0$ regions, e.g., $\mathbf{E}^{>+}$ denotes the front-wave $(y > 0)$, for $\rho > \rho_0$ region, evaluated on surface $S^>$. Note that the front-wave and back-wave concepts (delimited by plane $y = 0$) are only for notation convenience and they are different from the "physical" forward-propagating wave and the back-scattered wave (delimited by surface S), i.e., the forward-propagating wave is the front-wave $\mathbf{E}^{>+}$ and the back-scattered wave includes the front-wave $\mathbf{E}_<{}^+$ and the back-wave $\mathbf{E}^>{}_- = \mathbf{E}_{<-}$, which will be explained in details in Section 2.1.2.

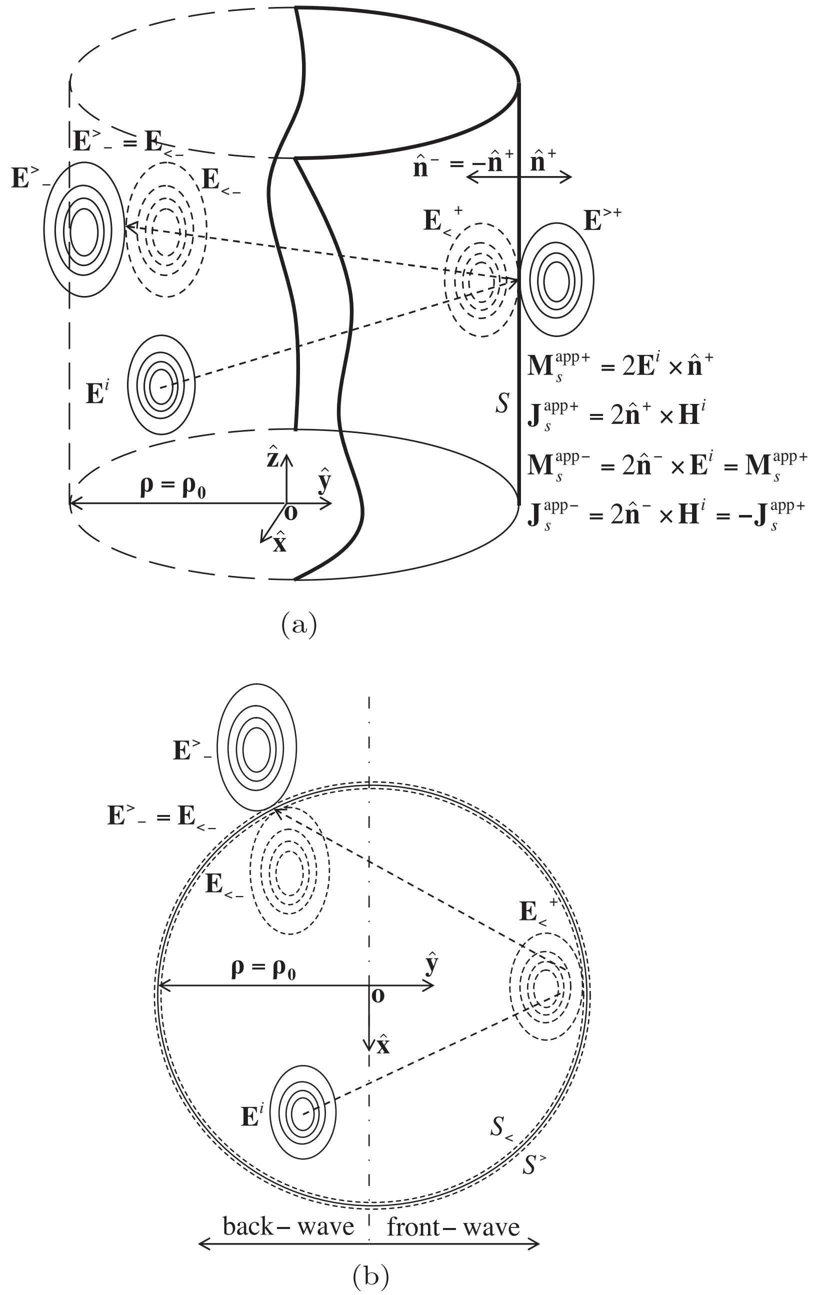

(a)

(b)

Figure 1. Electromagnetic wave propagation and scattering in the cylindrical geometry: (a) the side view; and (b) the top view.

2.1. The Vector Potential Method

In this section, the forward-propagating wave $\mathbf{E}^{>+}$ (back-scattered wave $\mathbf{E}_{<}{}^{+}$ and $\mathbf{E}^{>}{}_{-} = \mathbf{E}_{<-}$) in Fig. 1 is evaluated through the vector potential $\mathbf{F}$ and $\mathbf{A}$ for the given incident field $\mathbf{E}^{i}$. The comparison of the calculated forward-propagating wave $\mathbf{E}^{>+}$ (back-scattered wave $\mathbf{E}_{<}{}^{+}$ and $\mathbf{E}^{>}{}_{-} = \mathbf{E}_{<-}$) with the incident field $\mathbf{E}^{i}$ leads to the discrepancy parameter due to the image approximation.

2.1.1. The Cylindrical Harmonics

The cylindrical modal expansion of the vector potential $\mathbf{F}(\mathbf{r})$ for the magnetic current $\mathbf{M}_s(\mathbf{r}')$ on an arbitrary surface in the cylindrical coordinate is given as

$$\begin{aligned}\mathbf{F}(\mathbf{r}) &= \epsilon\iint_S [g(\mathbf{r}-\mathbf{r}')\mathbf{M}_s(\mathbf{r}')]\,dS' \\ &= \frac{\epsilon}{i8\pi}\iint_S\left[\mathbf{M}_s(\mathbf{r}')\int_{-\infty}^{\infty}H_0^{(2)}\left(\Lambda\left|\rho-\rho'\right|\right)e^{-ih(z-z')}dh\right]dS' \qquad (1)\end{aligned}$$

where ϵ is the permittivity of the homogeneous medium. $H_0^{(2)}(\,\cdot\,)$ is Hankel function of the second kind of order 0. The scalar Green's function $g(\,\cdot\,)$ and the transverse wave vector Λ are defined as

$$g(\,\cdot\,) = \frac{e^{-ik|\,\cdot\,|}}{4\pi|\,\cdot\,|}, \quad \Lambda = \sqrt{k^2-h^2}. \qquad (2)$$

According to the cylindrical addition theorem [17, 21],

$$\begin{aligned}H_0^{(2)}\left(\Lambda\left|\rho-\rho'\right|\right) &= H_0^{(2)}\left(\Lambda\sqrt{\rho^2+\rho'^2-2\rho\rho'\cos(\phi-\phi')}\right) \\ &= \sum_{m=-\infty}^{\infty}\left\{\begin{array}{l} H_m^{(2)}(\Lambda\rho)J_m(\Lambda\rho')e^{im(\phi'-\phi)}\Big|_{\rho>\rho'} \\ \\ J_m(\Lambda\rho)H_m^{(2)}(\Lambda\rho')e^{im(\phi'-\phi)}\Big|_{\rho<\rho'}\end{array}\right. \qquad (3)\end{aligned}$$

where $\rho \equiv |\rho|$ is the observation coordinate and $\rho' \equiv |\rho'|$ is the source coordinate. $J_m(\,\cdot\,)$ is Bessel function of the first kind of integer order m and $H_m^{(2)}(\,\cdot\,)$ is Hankel function of the second kind of integer order m. Substituting (3) into (1), the cylindrical modal expansion of $\mathbf{F}(\mathbf{r})$ on an arbitrary surface is obtained,

$$\mathbf{F}^{>}_{<}(\mathbf{r}) = \mathrm{IFT}\left(\mathbf{f}^{>}_{<}(m,h)\ \begin{matrix}H_m^{(2)}(\Lambda\rho)\\ J_m(\Lambda\rho)\end{matrix}\right)$$

$$\mathbf{f}^{>}_{<}(m,h) = \frac{\epsilon}{i4}\iint_S \left[\begin{array}{c} J_m(\Lambda\rho') \\ H_m^{(2)}(\Lambda\rho') \end{array} \mathbf{M}_s(\mathbf{r}')e^{i(m\phi'+hz')}\right] dS' \qquad (4)$$

where, the the superscript ">" denotes $\rho > \rho'$ and the subscript "<" denotes $\rho < \rho'$, similar to the definitions in Fig. 1. The Inverse Fourier Transform (IFT) is defined as

$$\mathrm{IFT}(\quad\cdot\quad) = \frac{1}{2\pi}\sum_{m=-\infty}^{\infty}\left\{\int_{-\infty}^{\infty}\left[(\quad\cdot\quad)\,e^{-i(m\phi+hz)}\quad\right]dh\right\}. \qquad (5)$$

The validity of (4) can be further confirmed by the Near-Field Far-Field (NF-FF) transform. The far-field $\mathbf{F}(\mathbf{r})|_{\text{FF}}$ can be obtained from (4) by letting $\rho \to \infty$,

$$\mathbf{F}^{>}(\mathbf{r})\big|_{\text{FF}} = \mathrm{IFT}\left(\ \mathbf{f}^{>}(m,h)H_m^{(2)}(\Lambda\rho)\ \right)\Big|_{\rho\to\infty} \qquad (6)$$

Also, for $\rho \to \infty$, the following relation holds [17],

$$\frac{1}{2\pi}\int_{-\infty}^{\infty}\left[\mathbf{f}^{>}(m,h)H_m^{(2)}(\Lambda\rho)e^{-ihz}\right]\Big|_{\rho\to\infty} dh = \frac{1}{\pi}\frac{e^{-ikr}}{r}i^{m+1}\,\mathbf{f}^{>}(m,h) \qquad (7)$$

Substituting (7) into (6),

$$\mathbf{F}^{>}(\mathbf{r})\big|_{\text{FF}} = \frac{1}{\pi}\frac{e^{-ikr}}{r}\sum_{m=-\infty}^{\infty}\left\{\ i^{m+1}\,\mathbf{f}^{>}(m,h)e^{-im\phi}\ \right\}. \qquad (8)$$

$\mathbf{F}(\mathbf{r})|_{\text{FF}}$ in (8) is the NF-FF transform in the cylindrical coordinate [22, 23], which can also be obtained from (1) by letting $\rho \to \infty$,

$$\mathbf{F}^{>}(\mathbf{r})\big|_{\text{FF}} = \epsilon\frac{e^{-ikr}}{4\pi r}\iint_S\left[\ \mathbf{M}_s(\mathbf{r}')e^{i\Lambda\rho'\cos(\phi-\phi')}e^{ihz'}\ \right]dS' \qquad (9)$$

Now, express $e^{i\Lambda\rho'\cos(\phi-\phi')}$ in a Fourier series [24],

$$e^{i\Lambda\rho'\cos(\phi-\phi')} = \sum_{m=-\infty}^{\infty}\left\{\ i^m J_m(\Lambda\rho')e^{-im(\phi-\phi')}\ \right\}. \qquad (10)$$

The substitution of (10) into (9) also gives (8).

Finally, the vector potential $\mathbf{A}(\mathbf{r})$ for the electric current $\mathbf{J}_s(\mathbf{r}')$ can be obtained through the duality relations,

$$\mathbf{E}\to\mathbf{H},\quad \mathbf{M}_s\to-\mathbf{J}_s,\quad \mathbf{F}\to-\mathbf{A},\quad \epsilon\to\mu. \qquad (11)$$

The result is given as

$$\begin{aligned}\mathbf{A}^{>}_{<}(\mathbf{r}) &= \mathrm{IFT}\left(\mathbf{g}^{>}_{<}(m,\,h)\ \begin{matrix} H_m^{(2)}(\Lambda\rho) \\ J_m(\Lambda\rho)\end{matrix}\right)\\ \mathbf{g}^{>}_{<}(m,\,h) &= \frac{\mu}{i4}\iint_S \left[\begin{matrix} J_m(\Lambda\rho') \\ H_m^{(2)}(\Lambda\rho')\end{matrix}\ \mathbf{J}_s(\mathbf{r}')e^{i(m\phi'+hz')}\right] dS'.\end{aligned}\tag{12}$$

2.1.2. The Forward-propagating Wave and Back-scattered Wave

In Fig. 1, $\mathbf{M}_s^{\mathrm{app}+}$ ($\mathbf{J}_s^{\mathrm{app}+}$) is the image approximation of the Love's equivalence principle for the electromagnetic wave propagation scenario and $\mathbf{M}_s^{\mathrm{app}-}$ ($\mathbf{J}_s^{\mathrm{app}-}$) is the image approximation of the induction equivalent (the physical equivalent) for the electromagnetic wave scattering scenario. It is not difficult to show that the following relations hold,

$$\mathbf{M}_s^{\mathrm{app}} = \mathbf{M}_s^{\mathrm{app}+} = 2(-\hat{\mathbf{n}}^{+}) \times \mathbf{E}^{i} = 2\hat{\mathbf{n}}^{-} \times \mathbf{E}^{i} = \mathbf{M}_s^{\mathrm{app}-}\ . \tag{13}$$

$$\mathbf{J}_s^{\mathrm{app}} = \mathbf{J}_s^{\mathrm{app}+} = 2\hat{\mathbf{n}}^{+} \times \mathbf{H}^{i} = -2\hat{\mathbf{n}}^{-} \times \mathbf{H}^{i} = -\mathbf{J}_s^{\mathrm{app}-}\ . \tag{14}$$

where $\hat{\mathbf{n}}^{+}$ ($\hat{\mathbf{n}}^{-}$) are the outward (inward) unit surface normals to S (see Fig. 1). The electromagnetic wave calculated from the equivalent current $\mathbf{M}_s^{\mathrm{app}}$ is thus the combination of the forward-propagating wave (front-wave $\mathbf{E}^{>+}$ in Fig. 1) and the back-scattered wave (the front-wave $\mathbf{E}_{<}^{+}$ and the back-wave $\mathbf{E}^{>}_{-} = \mathbf{E}_{<-}$ in Fig. 1). Physically, $\mathbf{E}^{>}_{-} = \mathbf{E}_{<-}$ because they are both evaluated on the back side of surface S (note that surface $S^{>}$ and surface $S_{<}$ are infinitesimally close to surface S). However, $\mathbf{E}^{>+} \neq \mathbf{E}_{<}^{+}$ due to the existence of the surface current $\mathbf{M}_s^{\mathrm{app}}$ on the front side of surface S. Similar argument holds for $\mathbf{J}_s^{\mathrm{app}}$ if the minus sign "$-$" between $\mathbf{J}_s^{\mathrm{app}+}$ and $\mathbf{J}_s^{\mathrm{app}-}$ is safely ignored without introducing any significant physical meaning.

Mathematically, for the narrow-band field, the separation of the forward-propagating wave and back-scattered wave is clear by noting that $J_m(\,\cdot\,)$ in (4) can be expressed as

$$J_m(\,\cdot\,) = \frac{H_m^{(1)}(\,\cdot\,) + H_m^{(2)}(\,\cdot\,)}{2} \tag{15}$$

where $H_m^{(1)}$ is the Hankel function of the first kind of integer order m. From (4), the front-wave and back-wave are given as

$$
\begin{aligned}
\mathbf{F}^{>+}_{<}(\mathbf{r}) &= \mathrm{IFT}\left(\mathbf{f}^{>+}_{<}(m,\,h)\ \begin{array}{c} H^{(2)}_m(\Lambda\rho) \\ H^{(1)}_m(\Lambda\rho) \end{array}\right) \\
\mathbf{F}^{>}_{<-}(\mathbf{r}) &= \mathrm{IFT}\left(\mathbf{f}^{>}_{<-}(m,\,h)H^{(2)}_m(\Lambda\rho)\right) \\
\mathbf{f}^{>+}_{<}(m,\,h) &= \frac{\epsilon}{i8}\iint_S \left[\begin{array}{c} H^{(1)}_m(\Lambda\rho') \\ H^{(2)}_m(\Lambda\rho') \end{array}\ \mathbf{M}^{\mathrm{app}}_s(\mathbf{r'})e^{i(m\phi'+hz')}\right] dS'. \\
\mathbf{f}^{>}_{<-}(m,\,h) &= \frac{\epsilon}{i8}\iint_S \left[H^{(2)}_m(\Lambda\rho')\mathbf{M}^{\mathrm{app}}_s(\mathbf{r'})e^{i(m\phi'+hz')}\right] dS'. \qquad (16)
\end{aligned}
$$

Now, suppose the incident field $\mathbf{E}^i(\rho_0)$ on the initial cylindrical surface S with a radius of ρ_0 is given as the combination of the TE and TM cylindrical harmonics [17, 19, 20],

$$
\mathbf{E}^i(\rho_0) = \sum_m \left\{\int_{-\infty}^{\infty}\left[a^h_m\ \mathbf{M}^{h>}_m(\rho_0) + b^h_m\ \mathbf{N}^{h>}_m(\rho_0)\right] dh\right\} \qquad (17)
$$

$$
\psi^{h>}_{m<}(\mathbf{r}) = \begin{array}{c} H^{(2)}_m(\Lambda\mathbf{r}) \\ J_m(\Lambda\mathbf{r}) \end{array}\ e^{-i(m\phi+hz)}, \quad \mathbf{L}^{h>}_{m<}(\mathbf{r}) = \nabla\left[\psi^{h>}_{m<}(\mathbf{r})\right], \qquad (18)
$$

$$
\mathbf{M}^{h>}_{m<}(\mathbf{r}) = \nabla\times\left[\hat{\mathbf{z}}\psi^{h>}_{m<}(\mathbf{r})\right], \quad \mathbf{N}^{h>}_{m<}(\mathbf{r}) = \frac{1}{k}\nabla\times\left[\mathbf{M}^{h>}_{m<}(\mathbf{r})\right]. \qquad (19)
$$

Due to the similarity, let's consider the $\mathbf{M}^{\mathrm{app}}_s$ image approximation. From (13) and (18)–(19), the equivalent magnetic current $\mathbf{M}^{\mathrm{app}}_s(\rho_0)$ on the cylindrical surface S ($\hat{\mathbf{n}}^+ = \hat{\rho}_0$) is given as

$$
\begin{aligned}
\mathbf{M}^{\mathrm{app}}_s(\rho_0) = 2\sum_{m'}\Bigg\{\int_{-\infty}^{\infty}\Bigg[e^{-i(m'\phi'+h'z')}\Bigg(a^{h'}_{m'}\left.\frac{\partial H^{(2)}_{m'}(\Lambda'\rho)}{\partial\rho}\right|_{\rho_0}\hat{\mathbf{z}}' \\
+\ b^{h'}_{m'}H^{(2)}_{m'}(\Lambda'\rho_0)\left(\frac{\Lambda'^2}{k}\hat{\phi}' + \frac{m'h'}{k\rho_0}\hat{\mathbf{z}}'\right)\Bigg)\Bigg] dh'\Bigg\} \qquad (20)
\end{aligned}
$$

The approximate field $\tilde{\mathbf{E}}^{>}_{<}(\mathbf{r})$ can be obtained from (4),

$$
\begin{aligned}
\tilde{\mathbf{E}}^{>}_{<}(\mathbf{r}) &= -\frac{1}{\epsilon}\left[\nabla\times\mathbf{F}^{>}_{<}(\mathbf{r})\right] \qquad (21) \\
\tilde{\mathbf{E}}^{>}_{<}(\mathbf{r}) &= \frac{-1}{2\pi\epsilon}\sum_m\left\{\int_{-\infty}^{\infty}\left(\mathbf{L}^{h>}_{m<}(\mathbf{r})\times\mathbf{f}^{>}_{<}(m,\,h)\right) d\right\} \qquad (22)
\end{aligned}
$$

The evaluation of (22) reduces to the calculation of $\mathbf{f}^{>}_{<}(m,h)$. Take $\mathbf{M}^{h>}_m$ (TE mode) as an example, on cylindrical surface S, from (4) and

(20),

$$\begin{aligned}\mathbf{f}^{\mathbf{TE}>}_{\mathrm{M}_s<}(m,h) &= \hat{\mathbf{z}}\sum_m\left\{\frac{\epsilon}{i2}\iint_S\left[e^{i(m\phi'+hz')}\ \begin{matrix}J_m(\Lambda\rho_0)\\ H_m^{(2)}(\Lambda\rho_0)\end{matrix}\right.\right.\\ &\qquad\left.\left.\times\left(a_m^h\left.\frac{\partial H_{m'}^{(2)}(\Lambda'\rho)}{\partial\rho}\right|_{\rho_0}e^{-i(m'\phi'+h'z')}\right)\right]dS'\right\}\\ &= \hat{\mathbf{z}}a_m^h\left(\frac{2\epsilon\pi^2\rho_0}{i}\right)\ \begin{matrix}J_m(\Lambda\rho_0)\\ H_m^{(2)}(\Lambda\rho_0)\end{matrix}\ \left.\frac{\partial H_m^{(2)}(\Lambda\rho)}{\partial\rho}\right|_{\rho_0}\end{aligned}\tag{23}$$

where the following relations have been used to derive (23),

$$\begin{aligned}\int_0^{2\pi}e^{i(m-m')\,\phi'}d\phi'=2\pi\delta_m^{m'}&=\begin{cases}2\pi & m'=m\\ 0 & m'\neq m\end{cases}\\ \int_{-\infty}^{\infty}e^{i(h-h')\,z'}dz'=2\pi\delta_h^{h'}&=\begin{cases}2\pi & h'=h\\ 0 & h'\neq h\end{cases}\end{aligned}\tag{24}$$

From (22), the approximate field $\tilde{\mathbf{E}}^{\mathrm{TE}\,>}_{\mathrm{M}_s<}(\rho_0)$ for TE mode is obtained as

$$\begin{aligned}\tilde{\mathbf{E}}^{\mathrm{TE}\,>}_{\mathrm{M}_s<}(\rho_0) &= \frac{-1}{2\pi\epsilon}\sum_m\left\{\int_{-\infty}^{\infty}\left[\ \mathrm{L}^{h>}_{\phi m<}(\rho_0)\mathrm{f}^{\mathrm{TE}>}_{z\mathrm{M}_s<}(m,h)\hat{\rho}_0\right.\right.\\ &\qquad\left.\left.-\ \mathrm{L}^{h>}_{\rho m<}(\rho_0)\mathrm{f}^{\mathrm{TE}>}_{z\mathrm{M}_s<}(m,h)\hat{\phi}\ \right]dh\right\}\end{aligned}\tag{25}$$

where $\mathrm{f}^{\mathrm{TE}>}_{z\mathrm{M}_s<}=\mathbf{f}^{\mathbf{TE}>}_{\mathrm{M}_s<}\cdot\hat{\mathbf{z}}$. Substitute (18) and (23) into (25),

$$\tilde{\mathbf{E}}^{\mathrm{TE}>}_{\mathrm{M}_s<}(\rho_0) = \sum_m\left\{\int_{-\infty}^{\infty}a_m^h\left[\xi^{\mathrm{TE}\,>}_{\rho\mathrm{M}_s<}\ \mathrm{M}^{h>}_{\rho m}(\rho_0)\hat{\rho}_0+\ \xi^{\mathrm{TE}\,>}_{\phi\mathrm{M}_s<}\ \mathrm{M}^{h>}_{\phi m}(\rho_0)\hat{\phi}\right]dh\right\}\tag{26}$$

$$\xi^{\mathrm{TE}\,>}_{\tau\mathrm{M}_s}\ =\ \xi^{\mathrm{TE}}_{\rho\mathrm{M}_s<}=\xi^{+}+\xi_{-},\qquad \xi^{\mathrm{TE}}_{\phi\mathrm{M}_s<}=-\left(\xi^{+}\right)^{*}+\xi_{-},\tag{27}$$

where, $\tau=\rho,\phi$ (TE mode) and ξ^{+}_{-} is defined as

$$\xi^{+}_{-}=\frac{i\pi\rho_0}{2}\ \begin{matrix}H_m^{(1)}(\Lambda\rho_0)\ \left.\frac{\partial H_m^{(2)}(\Lambda\rho)}{\partial\rho}\right|_{\rho=\rho_0}\\[2ex] H_m^{(2)}(\Lambda\rho_0)\ \left.\frac{\partial H_m^{(2)}(\Lambda\rho)}{\partial\rho}\right|_{\rho=\rho_0}\end{matrix}\ .\tag{28}$$

The derivation for $\mathbf{N}_m^{h>}$ (TM mode) is a little lengthy, which is shown in Appendix A. The result is,

$$\begin{aligned}\tilde{\mathbf{E}}^{\mathrm{TM}\,\gtrless}_{\mathbf{M}_s\,\lessgtr}(\rho_0) \;=\; \sum_m \Bigg\{\int_{-\infty}^{\infty} b_m^h \Bigg[\; & \xi^{\mathrm{TM}\,\gtrless}_{\rho\mathbf{M}_s\lessgtr}\;\mathrm{N}_{\rho m}^{\;h>}(\rho_0)\hat{\rho}_0 \\ & + \xi^{\mathrm{TM}\,\gtrless}_{\phi\mathbf{M}_s\lessgtr}\;\mathrm{N}_{\phi m}^{\;h>}(\rho_0)\hat{\phi} + \xi^{\mathrm{TM}\,\gtrless}_{z\mathbf{M}_s\lessgtr}\;\mathrm{N}_{zm}^{\;h>}(\rho_0)\hat{\mathbf{z}}\Bigg]dh\Bigg\} \qquad (29)\end{aligned}$$

$$\xi^{\mathrm{TM}\,>}_{\tau\mathbf{M}_s} = \xi^{\mathrm{TM}}_{\rho\mathbf{M}_s<} = \left(\xi^{+}\right)^{*} - \xi_{-}, \qquad \xi^{\mathrm{TM}}_{\phi\mathbf{M}_s<} = \xi^{\mathrm{TM}}_{z\mathbf{M}_s<} = -\xi^{+} - \xi_{-}. \qquad (30)$$

where, $\tau{=}\rho, \phi, z$ (TM mode). Comparing the calculated approximate field $\tilde{\mathbf{E}}^{\gtrless}_{\lessgtr} = \tilde{\mathbf{E}}^{\mathrm{TE}\,\gtrless}_{\mathbf{M}_s\lessgtr} + \tilde{\mathbf{E}}^{\mathrm{TM}\,\gtrless}_{\mathbf{M}_s\lessgtr}$ from (26) and (29) with the incident field $\mathbf{E}^i$ in (17), it is not difficult to see that the discrepancy parameters $\xi^{\mathrm{TE}\,\gtrless}_{\tau\mathbf{M}_s\lessgtr}$ and $\xi^{\mathrm{TM}\,\gtrless}_{\tau\mathbf{M}_s\lessgtr}$ ($\tau = \rho, \phi$ for TE mode and $\tau = \rho, \phi, z$ for TM mode) in (27) and (30) is due to the approximation of the image theorem. Similar to (16), it is not difficult to see from (27) and (30) that $\xi^{\mathrm{TE}\,\gtrless}_{\tau\mathbf{M}_s\lessgtr}$ and $\xi^{\mathrm{TM}\,\gtrless}_{\tau\mathbf{M}_s\lessgtr}$ can also be separated into the front-wave and back-wave parts as

$$\begin{aligned}\xi^{\mathrm{TE}\,>+}_{\tau\mathbf{M}_s} &= \xi^{\mathrm{TE}+}_{\rho\mathbf{M}_s<} = -\left[\xi^{\mathrm{TE}+}_{\phi\mathbf{M}_s<}\right]^{*} = \left[\xi^{\mathrm{TM}>+}_{\tau\mathbf{M}_s}\right]^{*} \\ &= \left[\xi^{\mathrm{TM}+}_{\rho\mathbf{M}_s<}\right]^{*} = -\xi^{\mathrm{TM}\,+}_{\phi\mathbf{M}_s<} = -\xi^{\mathrm{TM}\,+}_{z\mathbf{M}_s<} = \xi^{+}. &(31)\\ \xi^{\mathrm{TE}>}_{\tau\mathbf{M}_s-} &= \xi^{\mathrm{TE}}_{\tau\mathbf{M}_s<-} = -\xi^{\mathrm{TM}\,>}_{\tau\mathbf{M}_s-} = -\xi^{\mathrm{TM}}_{\tau\mathbf{M}_s<-} = \xi_{-}. &(32)\end{aligned}$$

Finally, the discrepancy parameters for $\mathbf{J}_s^{\mathrm{app}}$ image approximation (comparison of the magnetic field $\mathbf{H}$) can be obtained from the duality relations given in (11). With the help of (14), it can be shown that the following relations hold for $\mathbf{J}_s^{\mathrm{app}}$ image approximation,

$$\begin{aligned}\left[\;\xi^{\mathrm{TE}\,>+}_{\tau\mathbf{J}_s}\right]^{*} &= -\left[\;\xi^{\mathrm{TE}\,+}_{\rho\mathbf{J}_s<}\right]^{*} = \xi^{\mathrm{TE}\,+}_{\phi\mathbf{J}_s<} = \xi^{\mathrm{TE}\,+}_{z\mathbf{J}_s<} \\ &= \xi^{\mathrm{TM}\,>+}_{\tau\mathbf{J}_s} = -\xi^{\mathrm{TM}\,+}_{\rho\mathbf{J}_s<} = \left[\;\xi^{\mathrm{TM}\,+}_{\phi\mathbf{J}_s<}\right]^{*} = \xi^{+}. &(33)\\ \xi^{\mathrm{TE}\,>}_{\tau\mathbf{J}_s\;\;-} &= \xi^{\mathrm{TE}}_{\tau\mathbf{J}_s<-} = -\xi^{\mathrm{TM}\,>}_{\tau\mathbf{J}_s\;\;-} = -\xi^{\mathrm{TM}}_{\tau\mathbf{J}_s<-} = \xi_{\,-}. &(34)\end{aligned}$$

2.2. The Dyadic Green's Function Method

The dyadic Green's function for the magnetic field in the cylindrical coordinate [19, 20, 25] is given as

$$\bar{\mathbf{G}}_{\mathrm{HM}_s{}^{>}_{<}}(\mathbf{r},\mathbf{r}') = -\frac{\hat{\rho}\hat{\rho}'}{k^2}\delta(\rho-\rho')$$
$$+\sum_m\left\{\int_{-\infty}^{\infty}\left[\frac{1}{i8\pi\Lambda^2}\begin{pmatrix}\mathbf{M}_m^{h>}(\mathbf{r})\left[\mathbf{M}_{m<}^{h}(\mathbf{r}')\right]^*+\mathbf{N}_m^{h>}(\mathbf{r})\left[\mathbf{N}_{m<}^{h}(\mathbf{r}')\right]^* \\ \\ \mathbf{M}_{m<}^{h}(\mathbf{r})\left[\mathbf{M}_m^{h>}(\mathbf{r}')\right]^*+\mathbf{N}_{m<}^{h}(\mathbf{r})\left[\mathbf{N}_m^{h>}(\mathbf{r}')\right]^*\end{pmatrix}\right]dh\right\} \quad (35)$$

The approximate field $\tilde{\mathbf{E}}^{>}_{<}(\mathbf{r})$ is thus obtained from (21),

$$\tilde{\mathbf{E}}^{>}_{<}(\mathbf{r}) = -\nabla\times\left\{\iint_S\left[\bar{\mathbf{G}}_{\mathrm{HM}_s{}^{>}_{<}}(\mathbf{r},\mathbf{r}')\cdot\mathbf{M}_s^{\mathrm{app}}(\mathbf{r}')\right]dS'\right\} \quad (36)$$

Also, from (18)–(19), the following relations hold,

$$\begin{aligned}&\nabla\times\left[\mathbf{M}_{m<}^{h>}(\mathbf{r})\left[\mathbf{M}_{m<}^{h>}(\mathbf{r}')\right]^*\cdot\mathbf{M}_s^{\mathrm{app}}(\mathbf{r}')\right]\\ =\ & k\left[\mathbf{N}_{m<}^{h>}(\mathbf{r})\left[\mathbf{M}_{m<}^{h>}(\mathbf{r}')\right]^*\cdot\mathbf{M}_s^{\mathrm{app}}(\mathbf{r}')\right] \quad (37)\\ &\nabla\times\left[\mathbf{N}_{m<}^{h>}(\mathbf{r})\left[\mathbf{N}_{m<}^{h>}(\mathbf{r}')\right]^*\cdot\mathbf{M}_s^{\mathrm{app}}(\mathbf{r}')\right]\\ =\ & k\left[\mathbf{M}_{m<}^{h>}(\mathbf{r})\left[\mathbf{N}_{m<}^{h>}(\mathbf{r}')\right]^*\cdot\mathbf{M}_s^{\mathrm{app}}(\mathbf{r}')\right] \quad (38)\end{aligned}$$

With the help of (37)–(38), substituting (35) into (36) and using the orthogonal property of the cylindrical modal functions on cylindrical surface S, Equation (36) reduces to,

$$\tilde{\mathbf{E}}^{>}_{<}(\rho_0) = \frac{ik}{4\pi\Lambda^2}\sum_m\left\{\int_{-\infty}^{\infty}\left[a_m^h\begin{matrix}\mathbf{M}_m^{h>}(\rho_0)\\ \mathbf{M}_{m<}^{h}(\rho_0)\end{matrix}\left(\iint_S\begin{matrix}[\mathbf{N}_{m<}^{h}(\rho_0)]^*\times\mathbf{M}_m^{h>}(\rho_0)\\ [\mathbf{N}_m^{h>}(\rho_0)]^*\times\mathbf{M}_m^{h>}(\rho_0)\end{matrix}\hat{\rho}_0\,dS'\right)\right.\right.$$
$$\left.\left.+\ b_m^h\begin{matrix}\mathbf{N}_m^{h>}(\rho_0)\\ \mathbf{N}_{m<}^{h}(\rho_0)\end{matrix}\left(\iint_S\begin{matrix}[\mathbf{M}_{m<}^{h}(\rho_0)]^*\times\mathbf{N}_m^{h>}(\rho_0)\\ [\mathbf{M}_m^{h>}(\rho_0)]^*\times\mathbf{N}_m^{h>}(\rho_0)\end{matrix}\cdot\hat{\rho}_0\,dS'\right)\right]dh\right\} \quad (39)$$

The evaluation of (39) is straightforward. Take $\tilde{\mathbf{E}}^{\mathrm{TE}}_{\mathbf{M}_s{}^{>}_{<}}(\rho_0)$ as an example and note that,

$$\begin{matrix}[\mathbf{N}_{m<}^{h}(\rho_0)]^*\times\mathbf{M}_m^{h>}(\rho_0)\\ [\mathbf{N}_m^{h>}(\rho_0)]^*\times\mathbf{M}_m^{h>}(\rho_0)\end{matrix}\cdot\hat{\rho}_0 = \frac{\Lambda^2}{k}\frac{\partial H_m^{(2)}(\Lambda\rho)}{\partial\rho}\Bigg|_{\rho_0}\begin{matrix}J_m(\Lambda\rho_0)\\ H_m^{(2)}(\Lambda\rho_0)\end{matrix} \quad (40)$$

Substitute (40) into (39), $\tilde{\mathbf{E}}^{\mathrm{TE}}_{\mathbf{M}_s{}^{>}_{<}}(\rho_0)$ in (26) is also obtained. Following the similar procedure, equations (29)–(34) can be derived.

2.3. The Discrepancy Parameter due to the Image Approximation

When $\rho_0 \to \infty$, from (27)–(34), it is not difficult to see that $\xi^{\mathrm{TE}\,>}_{\tau\mathbf{M}_s\,<}$, $\xi^{\mathrm{TM}\,>}_{\tau\mathbf{M}_s\,<}$, $\xi^{\mathrm{TE}\,>}_{\tau\mathbf{J}_s\,<}$ and $\xi^{\mathrm{TM}\,>}_{\tau\mathbf{J}_s\,<}$ can be expressed in two quantities ξ^{+} and ξ_{-} defined in (28). For $\rho_0 \to \infty$, ξ^{+} approaches unit 1, which is expected. However, ξ_{-} shows oscillations, as can be seen from the property of Bessel function,

$$H_m^{(2)}(\Lambda\rho_0) = \left[\ H_m^{(1)}(\Lambda\rho_0)\ \right]^{*} \sim \sqrt{\frac{2i}{\pi\Lambda\rho_0}}\, i^{m} e^{-i\Lambda\rho_0},\ \ \rho_0 \to \infty, \tag{41}$$

From (41), ξ^{+} and ξ_{-} for $\rho_0 \to \infty$ reduce to

$$\xi^{+}\Big|_{(\rho_0\to\infty)} \to 1, \qquad \xi_{-}\Big|_{(\rho_0\to\infty)} \equiv \xi_{-}^{\infty} \to i(-1)^{m} e^{-i2\Lambda\rho_0}. \tag{42}$$

It is important to note that, although ξ_{-} (in the modal expansion coefficient) shows oscillation when $\rho_0 \to \infty$, the approximate field $\tilde{\mathbf{E}}^{\mathrm{TE}\,>}_{\mathbf{M}_s\,<}(\rho_0)$ in (26) and $\tilde{\mathbf{E}}^{\mathrm{TM}\,>}_{\mathbf{M}_s\,<}(\rho_0)$ in (29) have no such oscillation. Physically, the oscillation is due to the back-scattered wave $\mathbf{E}^{>}{}_{-} = \mathbf{E}_{<-}$ (see Fig. 1) evaluated on the back side of cylindrical surface S, which approaches 0 for $\rho_0 \to \infty$. Mathematically, the oscillation only appears in the modal expansion coefficients and disappears after the implementation of the sum and integration in (26) and (29). To look at this more carefully, let's consider the approximate field $\tilde{\mathbf{E}}^{\mathrm{TE}\,>}_{\mathbf{M}_s\,-}(\rho_0)$ for TE mode in (26),

$$\begin{aligned}&\tilde{\mathbf{E}}^{\mathrm{TE}\,>}_{\mathbf{M}_s\,-}(\rho_0,\phi)\\ &=\sum_m\left\{\int_{-\infty}^{\infty}\left[a_m^h\left(\xi^{\mathrm{TE}\,>}_{\rho\mathbf{M}_s\,-}\ \mathrm{M}_{\rho m}^{h>}(\rho_0)\hat{\rho}_0+\xi^{\mathrm{TE}\,>}_{\phi\mathbf{M}_s\,-}\ \mathrm{M}_{\phi m}^{h>}(\rho_0)\hat{\phi}\right)\right]dh\right\}\end{aligned} \tag{43}$$

Changing the variable $\phi' = \phi - \pi$ $(\hat{\phi}' = -\hat{\phi})$ and letting $\rho_0 \to \infty$,

$$\tilde{\mathbf{E}}^{\mathrm{TE}\,>}_{\mathbf{M}_s\,-}(\rho_0,\phi')\Big|_{(\rho_0\to\infty)} = \sum_m\left\{\int_{-\infty}^{\infty}\left[ia_m^h\ \mathbf{M}_m^{h>}(\rho_0)e^{-i2\Lambda\rho_0}\ \right]dh\right\} \tag{44}$$

Now, the back-scattered field $\tilde{\mathbf{E}}^{\mathrm{TE}\,>}_{\mathbf{M}_s\,-}(\rho_0 \to \infty, \phi') \to 0$ due to the fast variation of the phase term $e^{-i2\Lambda\rho_0}$, which means that the oscillation of ξ_{-} (in the modal expansion coefficient) doesn't appear in the actual field evaluation for $\rho_0 \to \infty$.

Due to the above reasons, ξ^+ is the discrepancy parameter of interest for the narrow-band beam scattering and diffraction in the open cylindrical surface, which is rewritten as follows,

$$\xi^+ = \frac{i\pi\rho_0}{2} H_m^{(1)}(\Lambda\rho_0) \left.\frac{\partial H_m^{(2)}(\Lambda\rho)}{\partial\rho}\right|_{\rho=\rho_0} \tag{45}$$

2.4. The Correction to the Image Approximation

For the open PEC cylindrical surface, the exact equivalent magnetic and electric surface currents $(\mathbf{M}_s^\pm, \mathbf{J}_s^\pm)$ can be found through the Electric Field Integral Equation (EFIE) or Magnetic Field Integral Equation (MFIE) [26, 27], with the help of (26) and (29). For EFIE, only the front-wave on the cylindrical surface, i.e., $\tilde{\mathbf{E}}_<^{>+}(\rho_0)$, is considered, which should satisfy the boundary condition on the inner/outer (-/+) cylindrical surface, i.e., $\hat{\mathbf{n}}^\pm \times \tilde{\mathbf{E}}_<^{>+}(\rho_0) = \pm\hat{\mathbf{n}}^\pm \times \mathbf{E}^i(\rho_0)$. From (17), (26) and (29), it is not difficult to obtain the exact equivalent magnetic and electric surface currents $(\mathbf{M}_s^\pm, \mathbf{J}_s^\pm)$ as follows,

$$\mathbf{M}_s^\pm(\rho_0) = -2\hat{\rho}_0 \times \sum_m \left\{ \int_{-\infty}^{\infty} \left[\frac{a_m^h}{\xi^+} \mathbf{M}_m^{h>}(\rho_0) + \frac{b_m^h}{(\xi^+)^*} \mathbf{N}_m^{h>}(\rho_0) \right] dh \right\}. \tag{46}$$

$$\mathbf{J}_s^\pm(\rho_0) = \pm\frac{i2}{\eta}\hat{\rho}_0 \times \sum_m \left\{ \int_{-\infty}^{\infty} \left[\frac{a_m^h}{(\xi^+)^*} \mathbf{N}_m^{h>}(\rho_0) + \frac{b_m^h}{\xi^+} \mathbf{M}_m^{h>}(\rho_0) \right] dh \right\}. \tag{47}$$

It can be seen from (13), (14) and (46), (47) that the image approximation $(\mathbf{M}_s^{\text{app}}, \mathbf{J}_s^{\text{app}})$ deviate from the exact equivalent surface currents $(\mathbf{M}_s^\pm, \mathbf{J}_s^\pm)$ by a factor of $\frac{1}{\xi^+}$ or $\frac{1}{(\xi^+)^*}$, in the cylindrical harmonics context. According to the property of the Fourier transform, (46) and (47) can also be expressed as the convolution of the spatial functions $\text{IFT}\left(\frac{1}{\xi^+}\right)$ or $\text{IFT}\left(\frac{1}{(\xi^+)^*}\right)$ with the corresponding (image) approximate equivalent surface currents $(\mathbf{M}_s^{\text{app}}, \mathbf{J}_s^{\text{app}})$. For a large radius ρ_0, $\text{IFT}\left(\frac{1}{\xi^+}\right)$ and $\text{IFT}\left(\frac{1}{(\xi^+)^*}\right)$ are δ-like functions and the coupling effect from the neighbored region is small. In particular, $\text{IFT}\left(\frac{1}{\xi^+}\right) \to \text{IFT}\left(\frac{1}{(\xi^+)^*}\right) \to \delta(\phi, z)$ for $\rho_0 \to \infty$, which means that the exact equivalent surface currents $(\mathbf{M}_s^\pm, \mathbf{J}_s^\pm)$ approach $(\mathbf{M}_s^{\text{app}}, \mathbf{J}_s^{\text{app}})$, which can be determined completely from the local electromagnetic field.

Table 1. The image approximation of Love's equivalence principle for $\rho > \rho'$.

$\rho > \rho'$	TE & $\mathbf{M}_s^{\text{app}}$	TM & $\mathbf{J}_s^{\text{app}}$
front-wave	$\xi_{\tau\mathbf{M}_s}^{\text{TE}>+} = \xi^+ \to [1]$	$\xi_{\tau\mathbf{J}_s}^{\text{TM}>+} = \xi^+ \to [1]$
back-wave	$\xi_{\tau\mathbf{M}_s-}^{\text{TE}>} = \xi_- \to [\xi_-^\infty]$	$\xi_{\tau\mathbf{J}_s-}^{\text{TM}>} = -\xi_- \to [-\xi_-^\infty]$
$\rho > \rho'$	TE & $\mathbf{J}_s^{\text{app}}$	TM & $\mathbf{M}_s^{\text{app}}$
front-wave	$\xi_{\tau\mathbf{J}_s}^{\text{TE}>+} = (\xi^+)^* \to [1]$	$\xi_{\tau\mathbf{M}_s}^{\text{TM}>+} = (\xi^+)^* \to [1]$
back-wave	$\xi_{\tau\mathbf{J}_s-}^{\text{TE}>} = \xi_- \to [\xi_-^\infty]$	$\xi_{\tau\mathbf{M}_s-}^{\text{TM}>} = -\xi_- \to [-\xi_-^\infty]$

Note: ξ_-^+ is defined in (28) and ξ_-^∞ is defined in (42); Quantities in $[\ \cdot\ ]$ are for $\rho_0 \to \infty$.

$\tau = \rho, \phi$ for (TE & $\mathbf{M}_s^{\text{app}}$) and (TM & $\mathbf{J}_s^{\text{app}}$); $\tau = \rho, \phi, z$ for (TE & $\mathbf{J}_s^{\text{app}}$) and (TM & $\mathbf{M}_s^{\text{app}}$).

Table 2. The image approximation of Love's equivalence principle for $\rho > \rho'$.

$\rho < \rho'$	TE & $\mathbf{M}_s^{\text{app}}$	TM & $\mathbf{J}_s^{\text{app}}$
front-wave		
ρ-part	$\xi_{\rho\mathbf{M}_s<}^{\text{TE}+} = \xi^+ \to [1]$	$\xi_{\rho\mathbf{J}_s<}^{\text{TM}+} = -\xi^+ \to [-1]$
ϕ-part	$\xi_{\phi\mathbf{M}_s<}^{\text{TE}+} = -(\xi^+)^* \to [-1]$	$\xi_{\phi\mathbf{J}_s<}^{\text{TM}+} = (\xi^+)^* \to [1]$
z-part	……	……
back-wave	$\xi_{\tau\mathbf{M}_s<-}^{\text{TE}} = \xi_- \to [\xi_-^\infty]$	$\xi_{\tau\mathbf{J}_s<-}^{\text{TM}} = -\xi_- \to [-\xi_-^\infty]$
$\rho < \rho'$	TE & $\mathbf{J}_s^{\text{app}}$	TM & $\mathbf{M}_s^{\text{app}}$
front-wave		
ρ-part	$\xi_{\rho\mathbf{J}_s<}^{\text{TE}+} = -(\xi^+)^* \to [-1]$	$\xi_{\rho\mathbf{M}_s<}^{\text{TM}+} = (\xi^+)^* \to [1]$
ϕ-part	$\xi_{\phi\mathbf{J}_s<}^{\text{TE}+} = \xi^+ \to [1]$	$\xi_{\phi\mathbf{M}_s<}^{\text{TM}+} = -\xi^+ \to [-1]$
z-part	$\xi_{z\mathbf{J}_s<}^{\text{TE}+} = \xi^+ \to [1]$	$\xi_{z\mathbf{M}_s<}^{\text{TM}+} = -\xi^+ \to [-1]$
back-wave	$\xi_{\tau\mathbf{J}_s<-}^{\text{TE}} = \xi_- \to [\xi_-^\infty]$	$\xi_{\tau\mathbf{M}_s<-}^{\text{TM}} = -\xi_- \to [-\xi_-^\infty]$

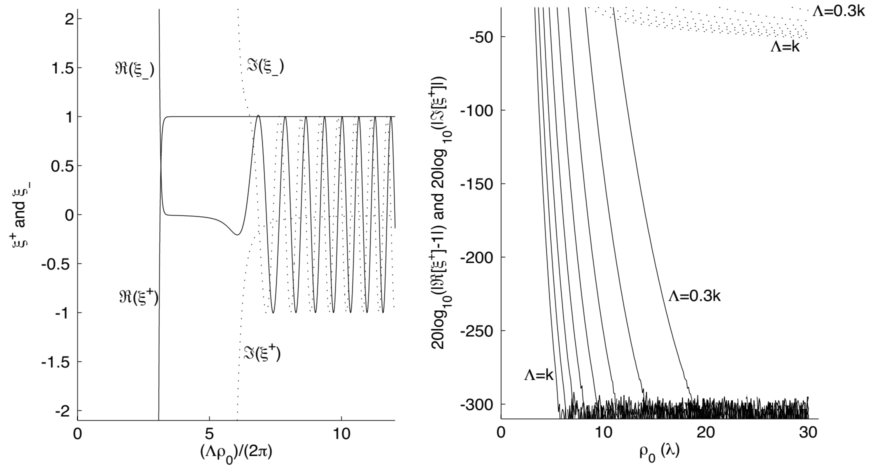

(a) (b)

Figure 2. Typical behavior of ξ^+ and ξ_- at $m = 40$: a) shows the asymptotic behavior of ξ^+ and ξ_- Vs. $\Lambda\rho_0$; and b) shows the dependence the real part $20\log_{10}(|1-\Re[\xi^+]|)$ and the imaginary part $20\log_{10}(|\Im[\xi^+]|)$ on ρ_0, for $\Lambda = 0.3k, 0.4k, \ldots, k$. In both plots, solid lines are for the real parts and dotted lines are for the imaginary parts.

Table 3. Threshold radii $\rho_{th}(\lambda)$ Vs. (m, h, Λ) for both the real and imaginary parts of ξ^+ (-30 dB accuracy).

			$\Im[\xi^+]$		
(h, Λ)/k	m = 0	m = 20	m = 40	m = 60	m = 80
(0, 1)	2.51	5.15	8.52	11.87	15.21
(0.2, 0.98)	2.56	5.26	8.69	12.12	15.52
(0.4, 0.92)	2.74	5.62	9.29	12.95	16.59
(0.6, 0.8)	3.14	6.44	10.64	14.84	19.01
(0.8, 0.6)	4.19	8.58	14.19	19.79	25.35
			$\Re[\xi^+]$		
(h, Λ)/k		m = 20	m = 40	m = 60	m = 80
(0, 1)		1.03	3.29	5.85	8.55
(0.2, 0.98)		1.05	3.35	5.97	8.73
(0.4, 0.92)		1.13	3.59	6.38	9.33
(0.6, 0.8)		1.29	4.11	7.31	10.69
(0.8, 0.6)		1.72	5.48	9.75	14.25

3. RESULT AND DISCUSSION

Table 1 and Table 2 summarize the properties and relations of $\xi^{\text{TE}\,>}_{\tau\mathbf{M}_s\,<}$, $\xi^{\text{TM}\,>}_{\tau\mathbf{M}_s\,<}$, $\xi^{\text{TE}\,>}_{\tau\mathbf{J}_s\,<}$ and $\xi^{\text{TM}\,>}_{\tau\mathbf{J}_s\,<}$, all of which can be expressed in two quantities, i.e., ξ^+ and ξ_-. When $\rho_0 \to \infty$, ξ^+ approaches ± 1 (-1 is due to the requirement of the PEC boundary condition for the electromagnetic wave scattering scenario, i.e., $\rho < \rho'$ on surface $S_<$ in Fig. 1) and ξ_- approaches 0 due to the fast phase variation $e^{-i2\Lambda\rho_0}$ in the approximate field evaluation (see Section 2.3 for explanation), which is expected for the image approximation, i.e., the image approximation approaches the exact solution for $\rho_0 \to \infty$.

Also, Fig. 2(a) shows the asymptotic behavior of ξ^+ and ξ_- Vs. $\Lambda\rho_0$, at $m = 40$, which confirms the analytical expressions given in (42). In Fig. 2(b), both the real part $20\log_{10}(|1 - \Re[\xi^+]|)$ and the imaginary part $20\log_{10}(|\Im[\xi^+]|)$ (also at $m = 40$) have been shown for different Λ, with respect to ρ_0 - it is clear that the imaginary part $\Im[\xi^+]$ dominates the accuracy of the image approximation. For the

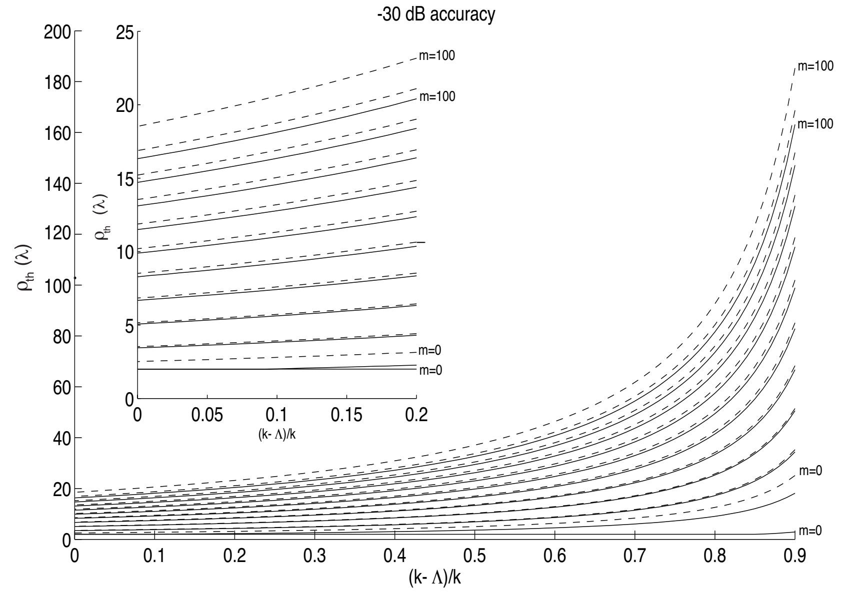

Figure 3. The normalized threshold radius ρ_{th} Vs. $(k - \Lambda)/k = 0$ to 0.9 ($\Lambda = 0.1k$ to k), for the $-30\,\text{dB}$ accuracy. Solid lines are for the magnitudes $20\log_{10}(|1 - |\xi^+||)$ and dashed lines are for the imaginary parts $20\log_{10}(|\Im[\xi^+]|)$. The narrow-band field region is enlarged in the inset plot for $(k - \Lambda)/k = 0$ to 0.2 ($\Lambda = 0.8k$ to k).

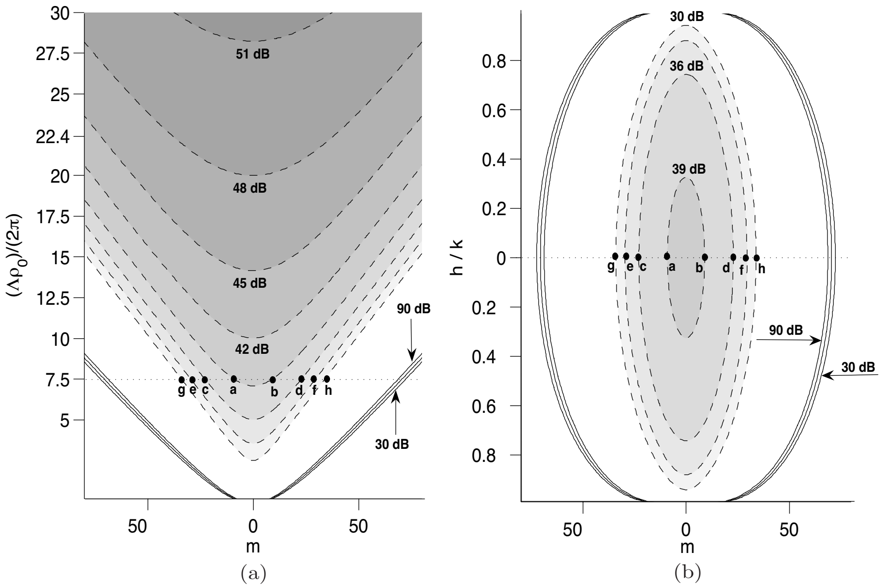

(a) (b)

Figure 4. The dB contour plot of discrepancy parameter ξ^+: a) for different m and $\Lambda\rho_0$; and b) for different m and h at $\rho_0 = 7.5\lambda$. Solid lines are for the real parts and dashed lines are for the imaginary parts. Plot a) and plot b) are connected through the dotted lines ($h = 0, \Lambda = k$), with selected boundary points denoted as (a,b), (c,d), (e,f) and (g,h) for ($-39, -36, -33, -30$) dB accuracies respectively.

given accuracy, it is possible to find the threshold radius ρ_{th} for different m and Λ, e.g., Fig. 3 shows such plot for the accuracy of -30 dB, from which it can be seen that the image approximation works well for mall m and h (large Λ), or equivalently, the narrow-band field.

Another way to look at the behavior of ξ^+ is to express it as a function of two parameters, i.e., m and $\Lambda\rho_0$, which can be seen from (45),

$$\begin{aligned} \xi^+ &= i\frac{\pi}{2}\left(\Lambda\rho_0\right) H_m^{(1)}(\Lambda\rho_0)\left.\frac{\partial H_m^{(2)}(\Lambda\rho)}{\partial\left(\Lambda\rho\right)}\right|_{\rho=\rho_0} \\ &= i\frac{\pi}{4}\left(\Lambda\rho_0\right) H_m^{(1)}(\Lambda\rho_0)\left[H_{m-1}^{(1)}(\Lambda\rho_0) - H_{m+1}^{(1)}(\Lambda\rho_0)\right] \end{aligned} \tag{48}$$

In Fig. 4(a), the dB contour plot of the real part (solid lines) and imaginary part (dashed lines) are shown for different accuracies, with respect to m and $\Lambda\rho_0$; also, Fig. 4(b) shows the dB contour plot of ξ^+ for $\rho_0 = 7.5\lambda$, with respect to m and $h = \sqrt{k^2 - \Lambda^2}$. Again, from both Fig. 4(a) and Fig. 4(b), it is clear that the imaginary part $\Im\left[\xi^+\right]$ dominates the accuracy and the image approximation works well for the narrow-band field (small m and h). Note that Fig. 4(a) and Fig. 4(b) are related to each other for $h = 0$ ($\Lambda = k$), which has been shown by the two dotted lines and the corresponding boundary points denoting different accuracies: (a, b) denotes $-39\,\mathrm{dB}$ imaginary part boundary ($|m| \sim 9$); (c, d) denotes $-36\,\mathrm{dB}$ imaginary part boundary ($|m| \sim 23$); (e, f) denotes $-33\,\mathrm{dB}$ imaginary part boundary ($|m| \sim 30$); and (g, h) denotes $-39\,\mathrm{dB}$ imaginary part boundary ($m \sim 34$). The real part boundary values are ($|m| \sim 69, 71, 72$) for ($-90\,\mathrm{dB}$, $-60\,\mathrm{dB}$, $-30\,\mathrm{dB}$) accuracies respectively. Also, Table 3 summarizes the corresponding threshold radii for -30 dB accuracy for different (m, h, Λ).

4. CONCLUSION

The discrepancy parameter due to the image approximation ($\mathbf{M}_s^{\mathrm{app}}$ and $\mathbf{J}_s^{\mathrm{app}}$ approximation) in the electromagnetic wave propagation scenario (Love's equivalence principle) and the electromagnetic wave scattering scenario (the induction equivalent and the physical equivalent) has been derived through two equivalent methods, i.e., the vector potential method and the dyadic Green's function method, in the cylindrical geometry, for both the TE and TM cylindrical harmonics. The accuracy of the image approximation depends on the property of the incident field (m, h, Λ), and the radius of the cylindrical surface (ρ_0): the narrow-band field and the cylindrical surface with a large radius give the high accuracy, e.g., to achieve $-30\,\mathrm{dB}$ accuracy, the imaginary part of the discrepancy parameter requires a threshold radius $\rho_{th} = 5.15\lambda$ for $(m, h, \Lambda) = (20, 0, k)$; however $\rho_{th} = 25.35\lambda$ is required for $(m, h, \Lambda) = (80, 0.8k, 0.6k)$. For the real part of the discrepancy parameter, the threshold radii are $\rho_{th} = 1.03\lambda$ for $(m, h, \Lambda) = (20, 0, k)$ and $\rho_{th} = 14.25\lambda$ for $(m, h, \Lambda) = (80, 0.8k, 0.6k)$. The closed-form formula of the discrepancy parameter is valuable for the evaluation of the validity of the image approximation for many applications including microwave imaging, RCS calculation, mirror system design and scattering phenomena in the cylindrical geometry.

ACKNOWLEDGMENT

This work was supported by the U.S. Dept. of Energy under the contract DE-FG02-85ER52122.

APPENDIX A. THE DISCREPANCY PARAMETER FOR TM MODE IN EQ. (29)

From (20), the equivalent magnetic surface current components $\mathrm{M}^{+}_{s\phi'}(\rho_0)$ and $\mathrm{M}^{+}_{sz'}(\rho_0)$ for $\mathbf{N}_m^{h>}(\rho_0)$ (TM mode) are given as

$$\mathrm{M}^{+}_{s\phi'}(\rho_0) = 2\sum_{m'}\left\{\int_{-\infty}^{\infty}\left[b_{m'}^{h'}\frac{\Lambda'^2}{k}H_{m'}^{(2)}(\Lambda'\rho_0)e^{-i(m'\phi'+h'z')}\right]dh'\right\} \tag{A1}$$

$$\mathrm{M}^{+}_{sz'}(\rho_0) = 2\sum_{m'}\left\{\int_{-\infty}^{\infty}\left[b_{m'}^{h'}\frac{m'h'}{k\rho_0}H_{m'}^{(2)}(\Lambda'\rho_0)e^{-i(m'\phi'+h'z')}\right]dh'\right\} \tag{A2}$$

Now covert the cylindrical coordinate into the rectangular coordinate,

$$\begin{aligned}\mathrm{M}^{+}_{sx'}(\rho_0) &= -\mathrm{M}^{+}_{s\phi'}(\rho_0)\sin\phi',\\ \mathrm{M}^{+}_{sy'}(\rho_0) &= \mathrm{M}^{+}_{s\phi'}(\rho_0)\cos\phi',\\ \mathrm{M}^{+}_{sz'}(\rho_0) &= \mathrm{M}^{+}_{sz'}(\rho_0)\end{aligned} \tag{A3}$$

The rectangular components of $\mathbf{f}_{\mathrm{M}_s}\gtrless(m,h)$ are thus evaluated as

$$\begin{aligned}&\mathrm{f}_x^{\mathrm{TM}}\gtrless(m,h) = \frac{\epsilon}{4}\sum_{m'}\Bigg\{\iint_S\Bigg[\begin{matrix}J_m(\Lambda\rho_0)\\ H_m^{(2)}(\Lambda\rho_0)\end{matrix}\; e^{i(m\phi'+hz')}\\ &\times\Bigg[b_{m'}^{h'}\frac{\Lambda'^2}{k}H_{m'}^{(2)}(\Lambda'\rho_0)e^{-ih'z'}\Big(e^{-i(m'-1)\phi'}-e^{-i(m'+1)\phi'}\Big)\Bigg]\Bigg]dS'\Bigg\}\end{aligned} \tag{A4}$$

$$\begin{aligned}&\mathrm{f}_y^{\mathrm{TM}}\gtrless(m,h) = \frac{\epsilon}{i4}\sum_{m'}\Bigg\{\iint_S\Bigg[\begin{matrix}J_m(\Lambda\rho_0)\\ H_m^{(2)}(\Lambda\rho_0)\end{matrix}\; e^{i(m\phi'+hz')}\\ &\times\Bigg[b_{m'}^{h'}\frac{\Lambda'^2}{k}H_{m'}^{(2)}(\Lambda'\rho_0)e^{-ih'z'}\Big(e^{-i(m'-1)\phi'}+e^{-i(m'+1)\phi'}\Big)\Bigg]\Bigg]dS'\Bigg\}\end{aligned} \tag{A5}$$

$$\begin{aligned}&\mathrm{f}_z^{\mathrm{TM}}\gtrless(m,h) = \frac{\epsilon}{i2}\sum_{m'}\Bigg\{\iint_S\Bigg[\begin{matrix}J_m(\Lambda\rho_0)\\ H_m^{(2)}(\Lambda\rho_0)\end{matrix}\; e^{i(m\phi'+hz')}\\ &\Bigg(b_{m'}^{h'}\frac{m'h'}{k\rho_0}H_{m'}^{(2)}(\Lambda'\rho_0)e^{-i(m'\phi'+h'z')}\Bigg)\;\Bigg]dS'\Bigg\}\end{aligned} \tag{A6}$$

On cylindrical surface S, from (24), $\mathbf{f}^{\text{TM}\gtrless}(m,\,h)$ is obtained as

$$\begin{aligned}\mathbf{f}^{\text{TM}\gtrless}(m,h)\big|_{\rho_0} = \;& \hat{\mathbf{x}}\left[\frac{\epsilon\pi^2\rho_0\Lambda^2}{k}\,\frac{J_m(\Lambda\rho_0)}{H_m^{(2)}(\Lambda\rho_0)}\right.\\ &\left.\left(b^{\,h}_{(m+1)}H^{(2)}_{m+1}(\Lambda\rho_0) - b^{\,h}_{(m-1)}H^{(2)}_{m-1}(\Lambda\rho_0)\right)\right]\\ &+\hat{\mathbf{y}}\left[\frac{\epsilon\pi^2\rho_0\Lambda^2}{ik}\,\frac{J_m(\Lambda\rho_0)}{H_m^{(2)}(\Lambda\rho_0)}\right.\\ &\left.\left(b^{\,h}_{(m+1)}H^{(2)}_{m+1}(\Lambda\rho_0) + b^{\,h}_{(m-1)}H^{(2)}_{m-1}(\Lambda\rho_0)\right)\right]\\ &+\hat{\mathbf{z}}\left[\frac{2\epsilon\pi^2 mh}{ik}\,\frac{J_m(\Lambda\rho_0)}{H_m^{(2)}(\Lambda\rho_0)}\,b^{h}_{m}H^{(2)}_{m}(\Lambda\rho_0)\right]\end{aligned} \tag{A7}$$

In the cylindrical coordinate,

$$\begin{aligned}\mathrm{f}_\rho^{\text{TM}}\gtrless(m,h)\Big|_{\rho_0} = \;& \frac{\epsilon\pi^2\rho_0\Lambda^2}{k}\,\frac{J_m(\Lambda\rho_0)}{H_m^{(2)}(\Lambda\rho_0)}\,\Big[b^{\,h}_{(m+1)}H^{(2)}_{m+1}(\Lambda\rho_0)e^{-i\phi}\\ &-b^{\,h}_{(m-1)}H^{(2)}_{m-1}(\Lambda\rho_0)e^{i\phi}\Big]\end{aligned} \tag{A8}$$

$$\begin{aligned}\mathrm{f}_\phi^{\text{TM}}\gtrless(m,h)\Big|_{\rho_0} = \;& \frac{\epsilon\pi^2\rho_0\Lambda^2}{ik}\,\frac{J_m(\Lambda\rho_0)}{H_m^{(2)}(\Lambda\rho_0)}\,\Big[b^{\,h}_{(m+1)}H^{(2)}_{m+1}(\Lambda\rho_0)e^{-i\phi}\\ &+b^{\,h}_{(m-1)}H^{(2)}_{m-1}(\Lambda\rho_0)e^{i\phi}\Big]\end{aligned} \tag{A9}$$

$$\mathrm{f}_z^{\text{TM}}\gtrless(m,h)\big|_{\rho_0} = \frac{2\epsilon\pi^2 mh}{ik}\,\frac{J_m(\Lambda\rho_0)}{H_m^{(2)}(\Lambda\rho_0)}\,b^{h}_{m}H^{(2)}_{m}(\Lambda\rho_0) \tag{A10}$$

Now from (22), the approximate field $\tilde{\mathbf{E}}^{\text{TM}}_{\text{M}_s}\gtrless(\rho_0)$ is given as

$$\begin{aligned}\tilde{\mathbf{E}}^{\text{TM}}_{\text{M}_s}\gtrless(\rho_0) &= \sum_m\left\{\int_{-\infty}^{\infty}\left[\;\tilde{\mathrm{N}}_\rho(\rho_0)\hat{\rho}_0 + \;\tilde{\mathrm{N}}_\phi(\rho_0)\hat{\phi} + \tilde{\mathrm{N}}_z(\rho_0)\hat{\mathbf{z}}\right]dh\right\}\\ \tilde{\mathrm{N}}_{\rho}^{\gtrless}(\rho_0) &= \frac{-1}{2\pi\epsilon}\left[\mathrm{L}^{h\gtrless}_{\phi m}(\rho_0)\mathrm{f}_z^{\text{TM}}\gtrless(m,h) - \mathrm{L}^{h\gtrless}_{zm}(\rho_0)\mathrm{f}_\phi^{\text{TM}}\gtrless(m,h)\right]\\ \tilde{\mathrm{N}}_{\phi}^{\gtrless}(\rho_0) &= \frac{-1}{2\pi\epsilon}\left[\mathrm{L}^{h\gtrless}_{zm}(\rho_0)\mathrm{f}_\rho^{\text{TM}}\gtrless(m,h) - \mathrm{L}^{h\gtrless}_{\rho m}(\rho_0)\mathrm{f}_z^{\text{TM}}\gtrless(m,h)\right]\\ \tilde{\mathrm{N}}_{z}^{\gtrless}(\rho_0) &= \frac{-1}{2\pi\epsilon}\left[\mathrm{L}^{h\gtrless}_{\rho m}(\rho_0)\mathrm{f}_z^{\text{TM}}\gtrless(m,h) - \mathrm{L}^{h\gtrless}_{\phi m}(\rho_0)\mathrm{f}_\rho^{\text{TM}}\gtrless(m,h)\right]\end{aligned} \tag{A11}$$

On cylindrical surface S, from (18)–(19) and (A9)–(A11),

$$\begin{aligned}\tilde{\mathrm{N}}^{\;>}_{\rho<}(\rho_0) =\, &\chi H_m^{(2)}(\Lambda\rho_0)J_m(\Lambda\rho_0)\Bigg[\; b_m^h\frac{2m^2h}{\rho_0}H_m^{(2)}(\Lambda\rho_0)\\ &-\rho_0\Lambda^2h\Big(b_{(m+1)}^{\;h}H_{m+1}^{(2)}(\Lambda\rho_0)e^{-i\phi}+b_{(m-1)}^{\;h}H_{m-1}^{(2)}(\Lambda\rho_0)e^{i\phi}\Big)\Bigg] \end{aligned}\tag{A12}$$

$$\begin{aligned}\tilde{\mathrm{N}}^{\;>}_{\phi<}(\rho_0) =\, &\chi\genfrac{}{}{0pt}{}{J_m(\Lambda\rho_0)}{H_m^{(2)}(\Lambda\rho_0)}\Bigg[\; i\rho_0\Lambda^2h\;\genfrac{}{}{0pt}{}{H_m^{(2)}(\Lambda\rho_0)}{J_m(\Lambda\rho_0)}\\ &\times\Big(b_{(m+1)}^{\;h}H_{m+1}^{(2)}(\Lambda\rho_0)e^{-i\phi}-b_{(m-1)}^{\;h}H_{m-1}^{(2)}(\Lambda\rho_0)e^{i\phi}\Big)\\ &-i2mh\;\genfrac{}{}{0pt}{}{\left.\frac{\partial H_m^{(2)}(\Lambda\rho)}{\partial\rho}\right|_{\rho_0}}{\left.\frac{\partial J_m(\Lambda\rho)}{\partial\rho}\right|_{\rho_0}}\; b_m^hH_m^{(2)}(\Lambda\rho_0)\Bigg]\end{aligned}\tag{A13}$$

$$\begin{aligned}\tilde{\mathrm{N}}^{\;>}_{z<}(\rho_0) =\, &\chi\;\genfrac{}{}{0pt}{}{J_m(\Lambda\rho_0)}{H_m^{(2)}(\Lambda\rho_0)}\;\Bigg[\; i\rho_0\Lambda^2\;\genfrac{}{}{0pt}{}{\left.\frac{\partial H_m^{(2)}(\Lambda\rho)}{\partial\rho}\right|_{\rho_0}}{\left.\frac{\partial J_m(\Lambda\rho)}{\partial\rho}\right|_{\rho_0}}\\ &\times\Big(b_{(m+1)}^{\;h}H_{m+1}^{(2)}(\Lambda\rho_0)e^{-i\phi}+b_{(m-1)}^{\;h}H_{m-1}^{(2)}(\Lambda\rho_0)e^{i\phi}\Big)\\ &-im\Lambda^2\genfrac{}{}{0pt}{}{H_m^{(2)}(\Lambda\rho_0)}{J_m(\Lambda\rho_0)}\;\Big(b_{(m+1)}^{\;h}H_{m+1}^{(2)}(\Lambda\rho_0)e^{-i\phi}\\ &-b_{(m-1)}^{\;h}H_{m-1}^{(2)}(\Lambda\rho_0)e^{i\phi}\Big)\Bigg]\end{aligned}\tag{A14}$$

where $\chi=\frac{\pi}{2k}=\frac{\lambda}{4}$. According to property of cylindrical Bessel function,

$$\frac{m}{\Lambda\rho_0}\;\genfrac{}{}{0pt}{}{J_m(\Lambda\rho_0)}{H_m^{(2)}(\Lambda\rho_0)}\;=\;\frac{1}{2}\;\genfrac{}{}{0pt}{}{J_{m-1}(\Lambda\rho_0)+J_{m+1}(\Lambda\rho_0)}{H_{m-1}^{(2)}(\Lambda\rho_0)+H_{m+1}^{(2)}(\Lambda\rho_0)}\tag{A15}$$

$$\genfrac{}{}{0pt}{}{\left.\frac{\partial J_m(\Lambda\rho)}{\partial(\Lambda\rho)}\right|_{\rho_0}}{\left.\frac{\partial H_m^{(2)}(\Lambda\rho)}{\partial(\Lambda\rho)}\right|_{\rho_0}}\;=\;\frac{1}{2}\;\genfrac{}{}{0pt}{}{J_{m-1}(\Lambda\rho_0)-J_{m+1}(\Lambda\rho_0)}{H_{m-1}^{(2)}(\Lambda\rho_0)-H_{m+1}^{(2)}(\Lambda\rho_0)}\tag{A16}$$

Substituting (A14)–(A16) into (A11) and collecting terms containing b_m^h, equation (29) is obtained.

REFERENCES

1. Booysen, A. J., "Aperture theory and the equivalence principle," *IEEE Antennas and Propagation Magazine*, Vol. 45, No. 3, 29–40, Jun. 2003.
2. Yaghjian, A. D., "Equivalence of surface current and aperture field integrations for reflector antennas," *IEEE Trans. on Antennas and Propagat.*, Vol. 32, Issue 12, 1355–1358, Dec. 1984.
3. Balanis, C. A., *Advanced Engineering Electromagnetics,* John Wiley & Sons, Inc., New York, 1989.
4. Lin, D.-B. and T.-H. Chu, "Bistatic frequency-swept microwave imaging: principle, methodology and experimental results," *IEEE Transactions on Microwave Theory and Techniques*, Vol. 41, No. 5, 855–861, May 1993.
5. Tseng, C.-H. and T.-H. Chu, "An effective usage of vector network analyzer for microwave imaging," *IEEE Transactions on Microwave Theory and Techniques*, Vol. 53, No. 9, 2884–2891, Sep. 2005.
6. Schlobohm, B., F. Amdt, and J. Kless, "Direct PO optimized dual-offset reflector antennas for small earth stations and for millimeter wave atmospheric sensors," *IEEE Transactions on Microwave Theory and Techniques*, Vol. 40, No. 6, 1310–1317, June 1992.
7. Galindo-Israel, V., W. A. Imbriale, and R. Mittra, "On the theory of the synthesis of single and dual offset shaped reflector antennas," *IEEE Trans. Antennas Propagat.*, Vol. AP-35, 887–896, Aug. 1987.
8. Hestilow, T. J., "Simple formulas for the calculation of the average physical optics RCS of a cylinder and a flat plate over a symmetric window around broadside," *IEEE Antennas and Propagation Magazine*, Vol. 42, No. 5, 48–52, Oct. 2000.
9. Adachi, S., A. Ohashi, and T. Uno, "Iterative radar target imaging based on modified extended physical optics method," *IEEE Trans. on Antennas and Propagat.*, Vol. 38, No. 6, 847–852, Jun. 1990.
10. Legault, S. R., "Refining physical optics for near-field computations," *Electronics Letters*, Vol. 40, No. 1, Jan. 8th, 2004.
11. Borkar, S. R. and R. F. H. Yang, "Reflection of electromagnetic waves from oscillating surfaces," *IEEE Trans. on Antennas and Propagat.*, 122–127, Jan. 1975.
12. Cramer, P. W. and W. A. Imbriale, "Speed up of near-field physical optics scattering calculations by use of the sampling theorem," *IEEE Transactions on Magnetics*, Vol. 30, No. 5, 3156–3159, Sep. 1994.

13. Cao, R. and R. J. Vernon, "Improved performance of three-mirror beam-shaping systems and application to step-tunable converters," *Joint 30th International Conference on Infrared and Millimeter Waves & 13th Internatioal Conference on Terahertz Electronics*, 616–617, Williamsburg, Virginia, USA, Sep. 19–23, 2005.
14. Perkins, M. P. and R. J. Vernon, "Iterative design of a cylinder-based beam-shaping mirror pair for use in a gyrotron internal quasi-optical mode converter," *29th International Conference on Infrared and Millimeter Waves*, Karlsruhe, Germany, Sep. 27–Oct. 1, 2004.
15. Liao, S. and R. J. Vernon, "A new fast algorithm for field propagation between arbitrary smooth surfaces," *Joint 30th Infrared and Millimeter Waves and 13th International Conference on Terahertz Electronics*, Vol. 2, 606–607, Williamsburg, Virginia, USA, 2005.
16. Liao, S. and R. J. Vernon, "Sub-THz beam-shaping mirror designs for quasi-optical mode converter in high-power gyrotrons," *J. Electromagn. Waves and Appl.*, scheduled for Vol. 21, No. 4, 425–439, 2007.
17. Harrington, R. F., *Time-harmonic Electromagnetic Fields*, McGraw-Hill, Inc., 1961.
18. Papa, R. J. and J. F. Lennon, "Conditions for the validity of physical optics in rough surface scattering," *IEEE Trans. on Antennas and Propagat.*, Vol. 36, No. 5, 647–650, May 1988.
19. Tai, C.-T., *The Dyadic Green's Function,* IEEE Press, 1991.
20. Collin, R. E., *Field Theory of Guided Waves*, second edition, IEEE Press, 1991.
21. Stratton, J. A., *Electromagnetic Theory*, McGraw-Hall, Inc., 1941.
22. Leach, Jr. W. M. and D. T. Paris, "Probe-compensated near-field measurements on a cylinder," *IEEE Trans. on Antennas and Propagat.*, Vol. 21, Issue 4, 435–445, Jul. 1973.
23. Yaghjian, A. D., "An overview of near-field antenna measurements," *IEEE Trans. on Antennas and Propagat.*, Vol. 34, Issue 1, 30–45, Jan. 1986.
24. Abramowitz, M. and I. A. Stegun, *Handbook of Mathematical Functions*, Dover, New York, 1965.
25. Li, L.-W., N.-H. Lim, W.-Y. Yin, and J.-A. Kong, "Eigenfunctional expansion of dyadic Green's functions in gyrotropic media using cylindrical vector wave functions," *Progress In Electromagnetics Research*, PIER 43, 101–121, 2003.

26. Gago, E. and M. F. Catedra, "Analysis of finite sized conducting patches in multilayer media using the CG-FFT method and discretizing Green's function in the spectral domain," *Progress In Electromagnetics Research*, PIER 05, 301–327, 1991.
27. Geyi, W., "New magnetic field integral equation for antenna system", *Progress In Electromagnetics Research*, PIER 63, 153–170, 2006.